Article

Surface Chemical Characterisation of Pyrite Exposed to *Acidithiobacillus ferrooxidans* and Associated Extracellular Polymeric Substances

Sian M. La Vars [1], Kelly Newton [1], Jamie S. Quinton [1], Pei-Yu Cheng [2], Der-Hsin Wei [2], Yuet-Loy Chan [2] and Sarah L. Harmer [1,*]

[1] Centre for Nanoscale Science and Technology, College of Science and Engineering, Flinders University, GPO Box 2100, Adelaide 5001, South Australia, Australia; lava0006@flinders.edu.au (S.M.L.V.); kell.newton@gmail.com (K.N.); jamie.quinton@flinders.edu.au (J.S.Q.)
[2] National Synchrotron Radiation Research Centre (NSRRC), 101 Hsin-Ann Road, Hsinchu Science Park, Hsinchu 30076, Taiwan; patrick3118619@hotmail.com (P.-Y.C.); dhw@nsrrc.org.tw (D.-H.W.); ylchan@retiree.nsrrc.org.tw (Y.-L.C.)
[*] Correspondence: sarah.harmer@flinders.edu.au; Tel.: +61-088-201-5338

Abstract: *A. ferrooxidans* and their metabolic products have previously been explored as a viable alternative depressant of pyrite for froth flotation; however, the mechanism by which separation is achieved is not completely understood. Scanning electron microscopy (SEM), photoemission electron microscopy (PEEM), time-of-flight secondary ion mass spectrometry (ToF-SIMS) and captive bubble contact angle measurements have been used to examine the surface physicochemical properties of pyrite upon exposure to *A. ferrooxidans* grown in HH medium at pH 1.8. C K-edge near edge X-ray absorption fine structure (NEXAFS) spectra collected from PEEM images indicate hydrophilic lipids, fatty acids and biopolymers are formed at the mineral surface during early exposure. After 168 h, the spectra indicate a shift towards protein and DNA, corresponding to an increase in cell population and biofilm formation on the surface, as observed by SEM. The Fe L-edge NEXAFS show gradual oxidation of the mineral surface from Fe(II) sulfide to Fe(III) oxyhydroxides. The oxidation of the iron species at the pyrite surface is accelerated in the presence of *A. ferrooxidans* and extracellular polymeric substances (EPS) as compared to HH medium controls. The surface chemical changes induced by the interaction with *A. ferrooxidans* show a significant decrease in surface hydrophobicity within the first 2 h of exposure. The implications of these findings are the potential use of EPS produced during early attachment of *A. ferrooxidans*, as a depressant for bioflotation.

Keywords: NEXAFS; PEEM; *A. ferrooxidans*; pyrite; ToF-SIMS; biofilm; EPS

1. Introduction

Gold- and copper-containing ore grades are declining, hence, suggesting the necessity for new and innovative processing procedures [1–4]. Copper sulfide minerals are abundant in nature and contain valuable base metals [1,4–7]. These copper sulfides are commonly associated with gangue materials of similar surface physicochemical properties [1,4–7]. One of the most common gangue materials is the iron sulfide mineral pyrite (FeS_2) [1–4]. The traditional method for separating pyrite from the valuable ore is froth flotation. This method is heavily dependent on the surface properties of the minerals being separated, requiring the materials of interest to be hydrophobic and for the gangue material to be hydrophilic, or vice versa [5–8]. In order to alter the surface properties of the sulfides, a variety of depressants, collectors, frothers and activators are used, many of which are undesirable to

work with due to their toxicity, flammability, instability and their potential for negative environmental impact [6,7].

Bioflotation is being thoroughly investigated, at the lab-scale, as an efficient, cost effective, environmentally friendly alternative to traditional froth flotation [9–11]. The bacterium *Acidithiobacillus ferrooxidans* has been of great interest to researchers as one of the most promising microbes for applications in bioflotation [11–15]. It is a non-pathogenic bacterium naturally found in areas where acid mine drainage occurs, utilizing ferrous iron and sulfur from the dissolution of sulfide minerals as sources of nutrients [11–15]. Three mechanisms describing the interaction of bacteria with sulfide minerals have been suggested: direct contact; indirect contact; and non-contact [16,17]. Both the direct contact and indirect contact mechanisms rely on the bacteria attaching to the mineral surface and forming a biofilm [16]. Extracellular polymeric substances (EPS) are excreted by bacteria as part of the cycle of adhesion providing binding sites for ferrous iron oxidation and aiding biofilm development [16,18–23]. Recent studies suggest that the EPS consists of carbohydrates, proteins, fatty acids, phosphorous, nucleic acids, uronic acids and humic acids [18,19,22]. The concentrations of which are affected by growth conditions and type of bacterium [20,23]. The *A. ferrooxidans* cells and their EPS have been found to contribute to hydrophobicity changes of the surfaces to which they attach, with polysaccharides decreasing [24,25], and proteins increasing hydrophobicity [26]. The concentration and time at which the polysaccharides and proteins are produced during biofilm formation is not well known and may impact the use of *A. ferrooxidans* for bioflotation.

The hydrophobicity of a mineral surface is dependent on the surface roughness and chemical heterogeneity of the first few atomic layers [5–7]. Traditional spectroscopic techniques including X-ray diffraction and fluorescence have depth penetrations in the order of microns. However, chemical changes that induce variations in surface hydrophobicity occur within the first 1–2 atomic layers. To determine the evolution of EPS components formed at mineral surfaces during biofilm formation more surface sensitive spectroscopic techniques are required [27]. Photoelectron Emission Microscopy (PEEM) offers several advantages over other spectroscopic techniques in the information it supplies. PEEM is a near surface technique with a sensitivity of 0.1–10 nm and a spatial resolution of down to 20 nm. Utilizing synchrotron light sources, tunable soft X-rays can be used to map specific chemical and elemental species on a surface through near-edge X-ray adsorption fine structure (NEXAFS) spectroscopy [28,29]. Time of flight secondary ion mass spectrometry (ToF-SIMS) enables the investigation of the composition of the outermost atomic layers of a surface that dictates hydrophobicity [30–33]. ToF-SIMS is a valuable technique that can also be used to "fingerprint" mixtures of large, complex biomolecules [33–36]. The combination of PEEM and ToF-SIMS with captive bubble contact angle measurements to determine surface hydrophobicity, may lead to the identification of the EPS components or cell coverage that decreases the hydrophobicity of pyrite upon exposure to *A. ferrooxidans*.

To this end, PEEM and ToF-SIMS have been used to identify and map the distribution of iron oxidation products and organic species produced by *A. ferrooxidans* in contact with pyrite over time. The aims are to: (i) identify the biopolymers and inorganic species produced during initial interaction, irreversible attachment, through to biofilm formation; (ii) correlate the surface speciation with changes in surface hydrophobicity of the mineral surface.

2. Materials and Methods

2.1. Culturing Microorganisms

The bacterial strain *A. ferrooxidans* (DSM 14887) was purchased from DSMZ (Leibniz-Institut DSMZ-Deutsche Sammlung von Mikroorganism und Zellkulturen) and grown on the recommended HH medium, DSMZ Medium 882. The medium consists of 0.132 g NH_4SO_4, 0.053 g $MgCl_2 \cdot 6H_2O$, 0.027 g KH_2PO_4, $CaCl_2$ $2H_2O$ in 1 L ultrapure water adjusted to pH 1.8 with H_2SO_4. 20 g of ground pyrite (+37 μm, −75 μm) was UV sterilised and added to sterile 500 mL conical flasks prior to inoculation by *A. ferrooxidans* at 10% inoculum. Cultures were grown in an orbital mixer shaken at

155 rpm at 30 °C, and continuously cultured every 4 days into fresh HH medium (5% inoculum) as a stock culture.

2.2. Pyrite Tile Preparation and Exposure to A. ferrooxidans

Accurate contact angle measurements require flat surfaces to prevent the interference of surface voids, cracks and particulates on the interaction between the surface and the bubble, such as bubble pinning [37]. PEEM requires smooth surfaces to prevent arcing due to the large potential difference between the sample and the electrostatic lens system. The smooth surface also allows for the determination of preferential attachment due to irreversible binding of bacteria to surfaces rather than physical containment in voids. For these reasons cubic pyrite (FeS_2) was cut to 1–2 mm thickness and 5 mm^2 in area and polished using wet/dry sand paper of increasingly fine grain size, then polished with 1 μm diamond paste. The tiles were sonicated for 3 min in ultrapure water and UV sterilized in a laminar flow hood prior to exposure experiments. *A. ferrooxidans* was inoculated at 10% inoculum into sterile HH medium containing the sterilised pyrite tiles with no additional iron source. The polished pyrite pieces were removed at 2, 24, 72 and 168 h. These exposure times were selected to reflect the initial interaction, irreversible binding of *A. ferrooxidans* cells on pyrite and biofilm formation. The samples were either analysed immediately or snap frozen in sterile HH medium, stored at −80 °C and kept frozen until ready for analysis. New tiles were used for each technique to prevent changes in surface speciation from exposure to X-rays, potential contamination during handling and oxidation at ambient conditions during transfer.

2.3. Scanning Electron Microscopy (SEM)

SEM allows the visualization and cell distribution across the surface of the mineral tiles and morphology of etch pits and secondary mineral precipitates during exposure to *A. ferrooxidans*. Pyrite tiles were removed from the cultures and stored in 3% glutaraldehyde at 4 °C prior to dehydration. The tiles were rinsed by immersion in phosphate buffered saline solution for 10 min and post-fixed by immersion in 1% osmium tetroxide for 30 min. The samples were then dehydrated by immersion in increasingly concentrated ethanol solutions for 10 min per rinse starting at 1 × 70% *v/v*, followed by 1 × 90% *v/v*, 1 × 95% *v/v* and 2 × 100% *v/v*, with a final rinse in hexamethyl-disilazane (HMDS) for 30 min [38,39]. Samples were then air dried and mounted to SEM stubs using carbon tape, and sputter coated with 3 nm of platinum.

Samples were analysed on either a Philips XL30 Field Emission Scanning Electron Microscope (FESEM) (Philips, Eindhoven, the Netherlands) or an Inspect FEI F50 Scanning Electron Microscope (FEI, Hillsboro, OR, USA) with a field emission electron emitter and EDX, backscatter, and secondary electron (SE) detectors. The primary electron beam accelerating voltage of 10 kV was used with spot size 3 when in Secondary Electron (SE) mode. Percentage cell coverage was calculated using the area of analysis, the number of cells absorbed on the surface and the average area of 6 individual cells using the image processing software "ImageJ" [40].

2.4. Captive Bubble Contact Angle

Captive bubble contact angle provides a measure of the wettability of a surface, and can be used to determine the hydrophobicity changes induced by bacteria and their EPS on mineral surfaces. Using the Captive bubble method rather than the Sessile drop method allows the EPS to remain in a natural hydrated state in solution, providing a more accurate measure of the wettability changes induced by the bacteria and their EPS in situ.

Pyrite tiles were removed from culture flasks and placed in the sterile HH medium to prevent drying before being loaded directly into the quartz cell for analysis. The samples were held face down and the sample face was immersed in solution. A J-shaped needle was positioned under the sample, through which air is pumped onto the surface. The volume of the bubble was increased over a period of approximately 60 s, with an image of the bubble captured after every volume increase to capture

the receding angles. The process was reversed to capture the advancing angles. Based on the captive bubble methods described in previous studies [41,42], the last five images taken before the bubble was removed from the surface were used for the advancing angle, and the central five images from the receding phase were used for the receding angle. These measurements were performed in triplicate and the standard deviation of these measurements used to assess reproducibility. To obtain the 0 h contact angle, a tile of polished pyrite was analysed by sessile drop at constant volume over a period of 2 min. Each contact angle was express as the angle between the solid and the air bubble for direct comparison. All Captive bubble contact angle experiments were performed using the Sinterface Profile Analysis Tensiometer PAT1 Version 8 (Sinterface, Berlin, Germany), and the contact angles from the images captured by the Sinterface PAT1 CCD camera were analysed using "ImageJ" imaging analysis software [43].

2.5. Photoemission Electron Microscopy (PEEM)

PEEM is a powerful spectromicroscopic technique, which combines high lateral resolution parallel imaging with near edge X-ray absorption spectroscopy for the chemical composition of surfaces. PEEM enables the identification and distribution of Fe and EPS speciation at the surface of pyrite through exposure to bacteria.

PEEM measurements were carried out on beamline BL05B2 (Scienta Omicron, Taunusstein, Germany) at the National Synchrotron Radiation Research Centre (NSRRC) in Hsinchu, Taiwan [28]. The beamline uses an elliptically polarized undulator (EPU5) and a spherical-grating monochromator, yielding very high photon flux of between 10^{11} and 10^{13} photons s^{-1} 200 $mÅ^{-1}$ over 60–1400 eV. The real-time, sample surface images were acquired by a Charge coupled device (CCD) detector behind a phosphor screen in total electron yield (TEY) mode, with the analysis chamber vacuum held at ultrahigh vacuum (1×10^{-9} Torr).

The PEEM images are 100 μm in diameter, with 8.1×10^5 pixels per image, with each pixel measuring 100 nm^2. Topographical effects were removed from the images by dividing by an image collected from a background region prior to the edge to remove background energy signals using "XSM reader" software [44]. C K-edge (280–300 eV) and Fe L-edge (699–730 eV) NEXAFS spectra were collected from regions on the pyrite surface selected using PEEM [44]. The Fe L-edge spectra were calibrated using standards of iron, Fe L_3 edge at 706.8 eV [45]. The C K-edge spectra were calibrated to the π* C=C eV peak of graphite at 285.4 eV [46] and to the π* C=O peak of bovine serum albumin (BSA) at 288.2 eV [47,48], respectively. All spectra were pre-edge and post-edge corrected by a linear pre- and post-edge fit using "Athena" software [49]. All spectra were normalized to the corrected pre- and post-edge regions.

2.6. Time of Flight-Secondary Ion Mass Spectrometry (ToF-SIMS)

ToF-SIMS is a surface sensitive technique that uses a pulsed ion beam to fragment ions from the first 1–2 atomic layers of a surface. The mass of those fragments is measured and provides elemental and chemical analysis of the surface. The ToF-SIMS experiments were performed using a Physical Electronics Inc. (Chanhassen, MN, USA) PHI TRIFT V nanoTOF instrument equipped with a pulsed liquid metal 79+Au primary ion gun (LMIG), operating at 30 kV energy. "Unbunched" beam settings were used to optimize spatial resolution. A cold stage was employed to prevent the loss of volatile species to the vacuum. A minimum temperature of −70 °C was reached and maintained for the duration of analysis. The mass spectra and images obtained by ToF-SIMS were calibrated using "WinCadenceN" software version 1.8.1.3 (PHI, Chanhassen, MN, USA). The mass spectra were calibrated to the CH_3^+, $C_2H_5^+$ and $C_3H_7^+$ peaks for positive ion mass spectra, and CH^-, C_2H^- and Cl^- peaks in the negative ion mass spectra. Both positive and negative spectra were collected over an area of 100 $μm^2$, with a minimum of 5 areas collected per sample. Integrated peak values of the selected ions were normalized to the total selected secondary ion intensities to correct for differences in the total ion yield between samples. Statistical analysis was carried out using a Student t-distribution

with 95% probability [30,50,51]. The results have been plotted using a 95% confidence interval and may be compared qualitatively.

To represent the hydrocarbons, carbohydrates and proteins present on the surface, positive fragments with little ambiguity as to their identity were selected to provide total proportion on the surface. For hydrocarbons, the fragments CH_3^+, $C_2H_3^+$, $C_2H_5^+$, $C_3H_3^+$, $C_3H_5^+$, $C_3H_7^+$, $C_4H_5^+$, $C_4H_7^+$, $C_4H_9^+$, $C_5H_3^+$, $C_5H_5^+$, $C_5H_7^+$, $C_6H_7^+$ and $C_6H_9^+$ are presented. For polysaccharides, the fragments CH_3O^+, $C_2H_5O^+$, $C_3H_7O^+$, $C_2H_5O_2^+$, $C_4H_5O^+$, $C_4H_7O^+$, $C_4H_9O^+$ and $C_3H_5O_3^+$ are presented. For proteins, the fragments CHN^+, CH_4N^+, $C_3H_6N^+$, $C_3H_5N_2^+$, $C_4H_8N^+$, $C_5H_{10}N^+$ and $C_5H_{12}N^+$ are presented. This method was used by Pradier [52], who determined carbohydrate and protein content by summing oxygenated and nitrogenated carbon signals, respectively. As the mass to charge ratio of the S_2^- and SO_2^- fragments are so close (*m/z* 63.941 and 63.962, respectively), the mass resolution is not sufficient to separate them, and so they are presented together as combined species.

3. Results

3.1. SEM

Typical SEM images of the pyrite controls and samples exposed to *A. ferrooxidans* for 2, 24, 72 and 168 h are shown in Figure 1. Over the first 24 h of exposure to *A. ferrooxidans*, mineral debris was observed on the surface of the pyrite and the pitting character was similar between the sample exposed to culture (Figure 1A,B) and HH medium (Figure 1E,F). Cells were observed on the surface after 2 h, and in greater numbers by 24 h, where they were observed reproducing by cell division on the surface, an example of which is indicated by arrows in Figure 1I. The cells seem to have no preference for site defects, as they were observed on all areas of the surface rather than concentrated around voids or cracks. There is evidence of pitting, typically regularly orientated and 0.8–1.8 μm in length and 0.2–0.8 μm wide. Scratches on the surface resulting from the polishing process, appear to be a nexus for the etch pits. Several studies observed etch pits similar in appearance to those seen in this study, with Gleisner [53] quantifying the pits dimensions and finding them to be 0.2–0.3 μm wide, which agrees with the etch pit dimensions found here [53–55]. After 72 h of exposure (Figure 1C), cells appear more concentrated around surface defects and voids. The pyrite surface shows "rivers" of cracks along crystal boundaries. These surface artefacts have been observed in a previous study by Karavaiko [56] who determined that they are not caused by direct bacterial action, but rather abiotic leaching along crystal boundaries. After 168 h (Figure 1D), advanced pitting can be observed as surface dissolution progresses. Additionally, cells appear in greater numbers on the surface, with bacterial colonies forming in all regions (Figure 1D).

The pyrite tiles exposed to HH medium (Figure 1E–H) show regularly orientated voids typical for natural specimens of pyrite that contain fluid inclusions, and scratches on the surface from the polishing process [57]. After 168 h of exposure (Figure 1H) significantly more etch pits are visible on the surface compared to earlier exposures (Figure 1E–G). The pyrite exposed to *A. ferrooxidans* shows significantly greater deterioration compared to the control at 72 h, with the appearance of larger etch pits and the formation of "rivers" of cracks that are not apparent on the control surface at any stage.

Studies that have compared bioleaching with abiotic controls agree with the comparatively smooth control surfaces observed in this study, suggesting the presence of cells accelerates pyrite leaching [58,59].
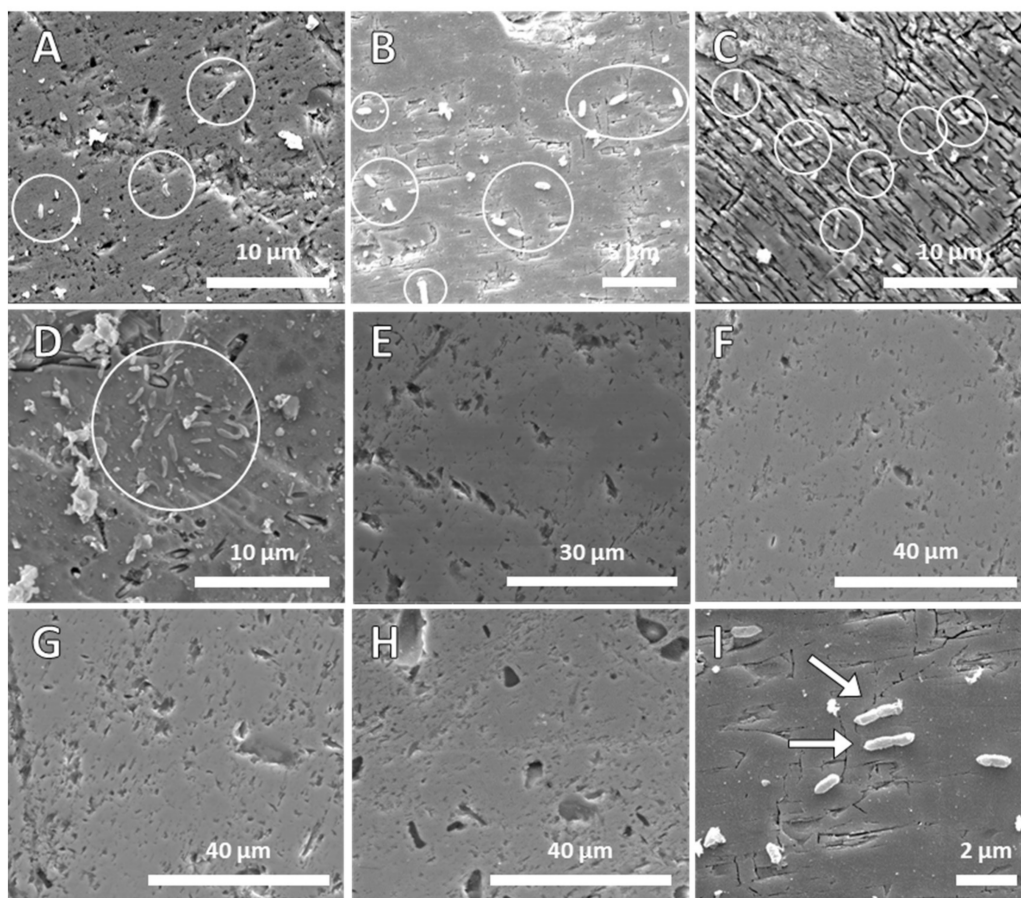
Figure 1. SEM micrographs of pyrite tiles exposed to *A. ferrooxidans* (indicated by circles) for (**A**) 2 h; (**B**) 24 h; (**C**) 72 h; (**D**) 168 h: pyrite tiles exposed to HH medium for (**E**) 2 h; (**F**) 24 h; (**G**) 72 h; (**H**) 168 h; (**I**) SEM micrograph of *A. ferrooxidans* cells in the process of cell division at 24 h.

3.2. Captive Bubble Contact Angle

The average of five advancing and receding contact angles for each pyrite sample, performed in triplicate, are shown in Figure 2, with the error bars representing the standard deviation of the samples measured. Pyrite samples exposed to *A. ferrooxidans* are more hydrophilic than the HH medium control at early stages of exposure, showing the most significant increase in hydrophilicity at 2 h, with differences in contact angles of 9°–18°. After 24 h, the pyrite exposed to *A. ferrooxidans* shows similar receding angle values to the sterile HH control; however, the advancing angle is more than 25° greater. This indicates the pyrite exposed to *A. ferrooxidans* is more homogenous at this period of exposure, suggesting improved hysteresis. After 72 h, the contact angles are similar for both control and bacteria-exposed pyrite, with the contact angle appearing to remain stable for 168 h.

These observations are supported by several previous studies that also suggest *A. ferrooxidans* reduces the hydrophobicity of pyrite, providing evidence through flotation results, or on air-dried samples rather than in situ contact angle measurements [54,60–62]. A difference in measured contact angle as little as 3° can alter mineral recovery by up to 18%, depending on the size fraction of the particles [4]. These results suggest that an exposure of as little as 2 h could promote the depression of pyrite by *A. ferrooxidans*, while longer periods of exposure showed no significant separation of contact angle compared to the sterile control sample. Although previous studies have reported that the depression of pyrite is reliant on the formation of a biofilm [5,6], these results suggest a biofilm is not necessary for significant changes in the hydrophilicity of pyrite, as the SEM showed little cell coverage after 2 h.
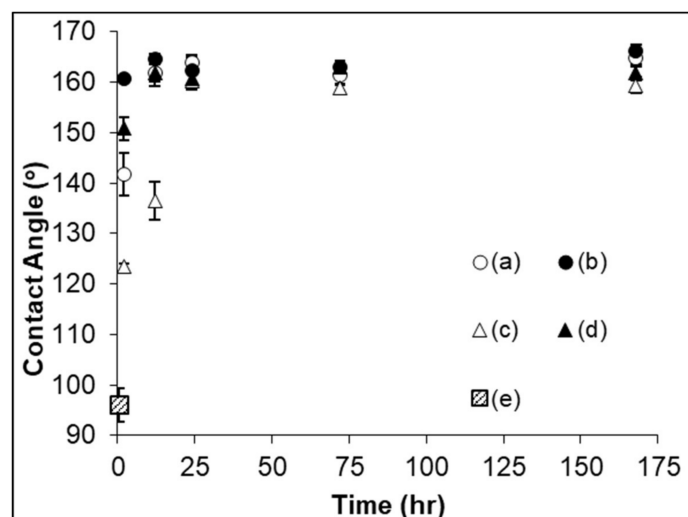
Figure 2. Surface wettability changes induced on pyrite by exposure to HH Medium and *A. ferrooxidans* over 168 h: The (a) advancing contact angle in HH medium; (b) receding contact angles in HH medium. (c) advancing contact angle when exposed to *A. ferrooxidans*; (d) receding contact angles when exposed to *A. ferrooxidans*; and (e) bare polished pyrite. Error bars represent sample the standard deviation in the contact angle measurements.

3.3. Fe L-edge PEEM and NEXAFS

The pyrite Fe L-edge NEXAFS spectra in Figure 3 show that the Fe L_3 peak is the most prominent feature, seen as two overlapping peaks due to transitions to the Fe 3*d* eg at 707.6 eV (A) and to Fe 3*d* states hybridized with S 3*p* at 708.5 eV (B) [63,64]. Two characteristic peaks at 712–715 eV (C) are due to transitions to S 3*p* states hybridized with Fe 4*s* and 4*p* states in pyrite, while the intense Fe L_2 peak resides at 719.9 eV (D) [63–66]. Iron oxidation products including hematite [45,67,68], magnetite [68], goethite [45,68], and wüstite [68] result in transitions of Fe 2*p* to Fe 3*d* states hybridized with O 2*p* states that overlap the pyrite Fe-S contributions between 707.8 and 710.5 eV.
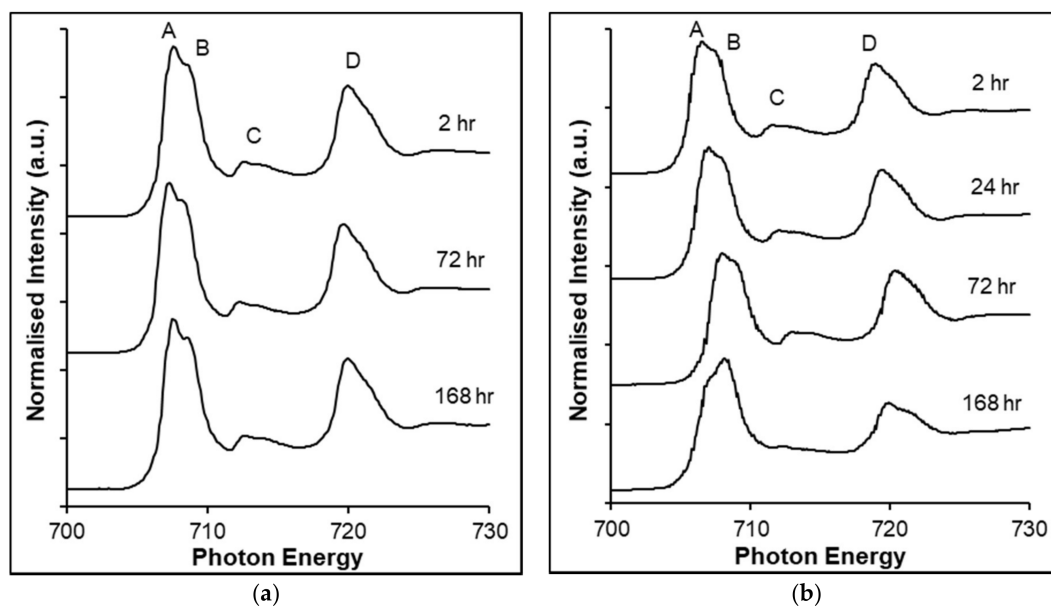

Figure 3. The surface iron speciation of pyrite after 2, 24, 72 and 168 h of exposure to: (**a**) HH medium; and (**b**) *A. ferrooxidans*.

Pyrite samples exposed to HH medium as a control, show no discernible changes in the features of the Fe L-edge spectra, from 2 to 168 h, Figure 3a. The NEXAFS spectra obtained for pyrite shown in Figure 3a, agree with those obtained by Goh [45] and are consistent with previous studies of synthetic and natural pyrite samples displaying unaltered pyrite [63,64]. The pyrite samples exposed to *A. ferrooxidans* show changes in spectral features between earlier exposure times and the 168 h exposure, Figure 3b. The peak at (B) corresponds to the Fe $3d$ states hybridized with S $3p$ and the overlapping iron oxides and oxyhydroxides, and increases over the course of exposure [63–66]. The two peaks at 712–715 eV (C) corresponding to bulk pyrite decrease over time, indicating a decrease in the bulk pyrite signal due to an increase in overlaying iron oxidation products [45,69].

The PEEM images collected at 707.6 eV and 708.5 eV corresponding to unaltered pyrite and Fe oxyhydroxides are show in Figure 4. The lighter regions indicate a higher concentration of iron species in certain regions, which are identical at both photon energies for each sample. The pyrite surface appears heterogeneous over the course of exposure, indicating that areas differ in iron concentration. The dark regions on the surface are likely due to the formation of sulfur-rich, oxygen-rich and iron-deficient species that form when pyrite is exposed to both air and acidic media [70–72]. There is no indication of increased oxidation of the control over the course of exposure, which supports the observations made using the NEXAFS spectra.
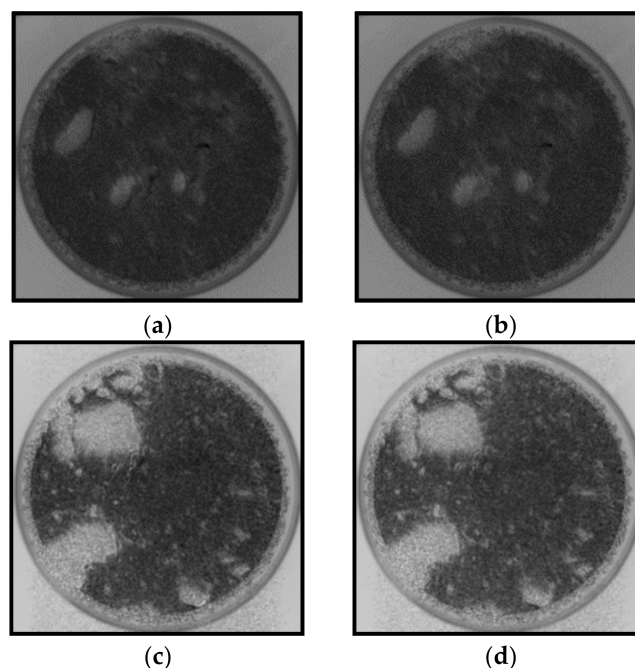

(**a**)　　　　　　　　　　　　　　　　　　　　(**b**)

(**c**)　　　　　　　　　　　　　　　　　　　　(**d**)

Figure 4. Single energy PEEM images showing the distribution of surface iron speciation on pyrite exposed to HH medium. The iron rich regions are light and iron deficient regions are dark. After 2 h of exposure (**a**) unaltered pyrite, 707.6 eV; (**b**) iron oxyhydroxides, 708.5 eV; and after 168 h (**c**) indicates unaltered pyrite and (**d**) iron oxyhydroxides.

3.4. C K-edge NEXAFS

Figure 5a shows the C K-edge NEXAFS spectra of pyrite exposed to HH medium for 2, 72 and 168 h. The peak at 285.1 eV can be attributed to the C 1s transitions to either π* C=C and/or π* C–H (A) [73,74]. The large, broad peak at 292 eV can be attributed π* C–C and σ* C–C, respectively (C) [74]. Peaks at 287.6 eV and 288.8 are due to σ* C–H (B) [75–77].

The C K-edge NEXAFS of the control pyrite surface exhibits little change over time. There are two possibilities; firstly, there is a large concentration of background adventitious carbon; secondly, there is the possibility of radiation damage occurring on the surface due to the incident photons. This

has been documented in previous NEXAFS studies as a characteristically intense C=C peak at 285.1 eV, that occurs as dehydrogenated C–H bonds [78,79]. The other peaks are all indicative of hydrocarbon structures containing no nitrogen or oxygen functionalities, which are highly likely to be adventitious due to the exposure to the atmosphere prior to loading the sample into the vacuum chamber and beamline, and is an unavoidable hazard of measuring carbon with all spectroscopic techniques of this nature [33,80].
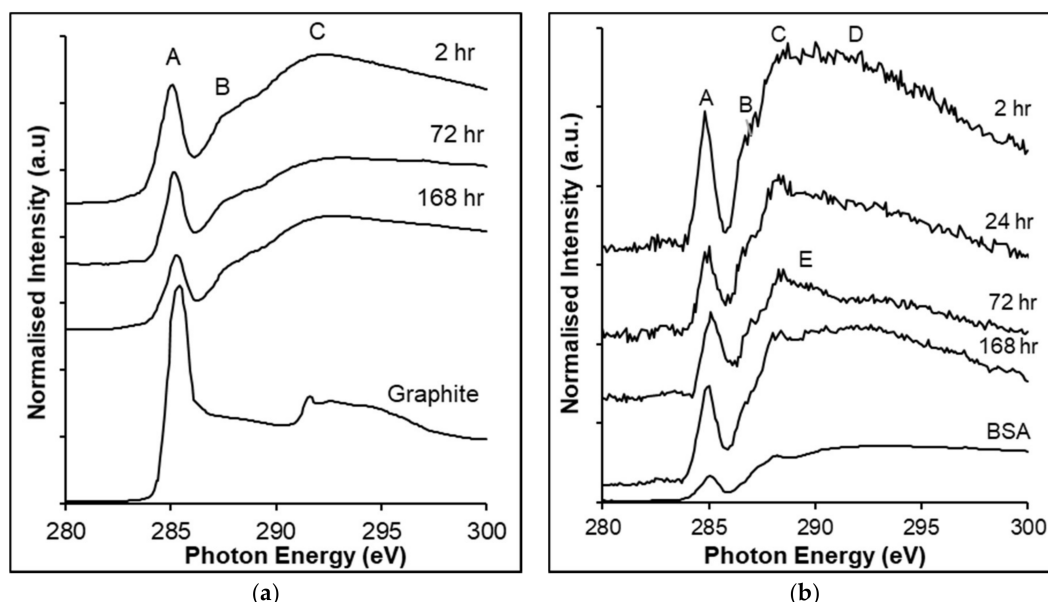

Figure 5. C K-edge NEXAFS spectra of (**a**) pyrite exposed to HH medium for 2, 72 and 168 h and graphite standard; (**b**) pyrite exposed to *A. ferrooxidans* for 2, 24, 72 and 168 h and a BSA standard. The peaks labelled A through E correspond to: (A) C 1s to π^* C=C and C–H from adventitious carbon: (B) π^* C=N and σ^* C–H; (C) π^* C=O carboxylic acids in lipids and biopolymers; (D) σ^* C–C; and (E) σ^* CNH, σ^* CH or π^* C=N, proteins and nucleic acids (E).

Figure 5b shows the stacked C K-edge NEXAFS spectra of pyrite exposed to *A. ferrooxidans* for 2, 24, 72 and 168 h, and the changes in the carbon species occurring over those exposure times. Each C K-edge NEXAFS spectrum of the pyrite samples exposed to *A. ferrooxidans* exhibits a peak at 285 eV due to C 1s transitions to π^* C=C and C–H (A). Peaks between 286 eV and 287.7 eV (B) can be attributed to both the C 1s transitions to π^* C=N and σ^* C–H [73–76,81–83]. The intensity of the π^* C=C peak at 285 eV (A) suggests that radiation damage may have occurred, reducing the signal from C–H and C–C peaks between 286–287.7 eV (B) and 292–294 eV (D) [78,79]. The presence of carbonate signal at 290 eV is also an indicator of possible radiation damage, as carboxyl and carbonyl groups are reduced to form carbonate species on the surface, where there is no source of carbonate in the HH medium solution or the pyrite sample [76,78,79].

The π^* C=O peak after 2 h occurs between 288.4–288.7 eV (C), suggesting that the peak is due to more carboxylic-type character common in lipids and biopolymer, that are likely to decrease the hydrophobicity of the surface at this stage [75,82–85]. In comparison, π^* C=O peak occurs at 288.2 eV (C) after 24 h and remains there for the remainder of exposure, suggesting this is due to the π^* C=O bonds in amides of protein [74–77,81,83,85]. The protein-type π^* C=O peak is commonly associated with the signal at 289.4 eV (E), which can be attributed to C 1s transitions to σ^* CNH, σ^* CH or π^* C=N amide functionality in proteins and nucleic acids [74,75,77].

After 168 h of exposure to bacteria, the shift in the π^* C=O peak at 288.2 eV (C) is also accompanied by an apparent increase in intensity in σ^* C–C at 292–294 eV (D). This indicates a further shift towards

polymeric substances, with fatty acids and nucleic acids becoming more prevalent on the surface as biofilm starts to build [74–76].

Few studies have investigated this system using NEXAFS, however, the C K-edge spectra of *A. ferrooxidans* cells collected by Mitsunobu [58] agree with the spectra collected in this study. They note that the protein signal at 288.2 eV was the most intense, with shoulders at approximately 287 eV and 289.4 eV that are also observed in the spectra found in this investigation.

3.5. ToF-SIMS

The ToF-SIMS statistics obtained from both positive and negative ion fragments of pyrite exposed to HH medium and *A. ferrooxidans* are shown in Figures 6 and 7. As the samples were analyzed using the same parameters, the intensities of the peaks can be used as a measure of the variation between samples. The positive and negative ion fragments contain a large number of peaks from both inorganic and organic species. The positive ions of interest were Fe, FeOH, C_xH_y, $C_xH_yO_z$ and $C_xH_yN_z$ and were collected at 2, 24, 72 and 168 h of exposure (Figure 6). The negative ions of interest were O, OH, S, SH, S_2, S_3, S_4, SO_3 (Figure 7).
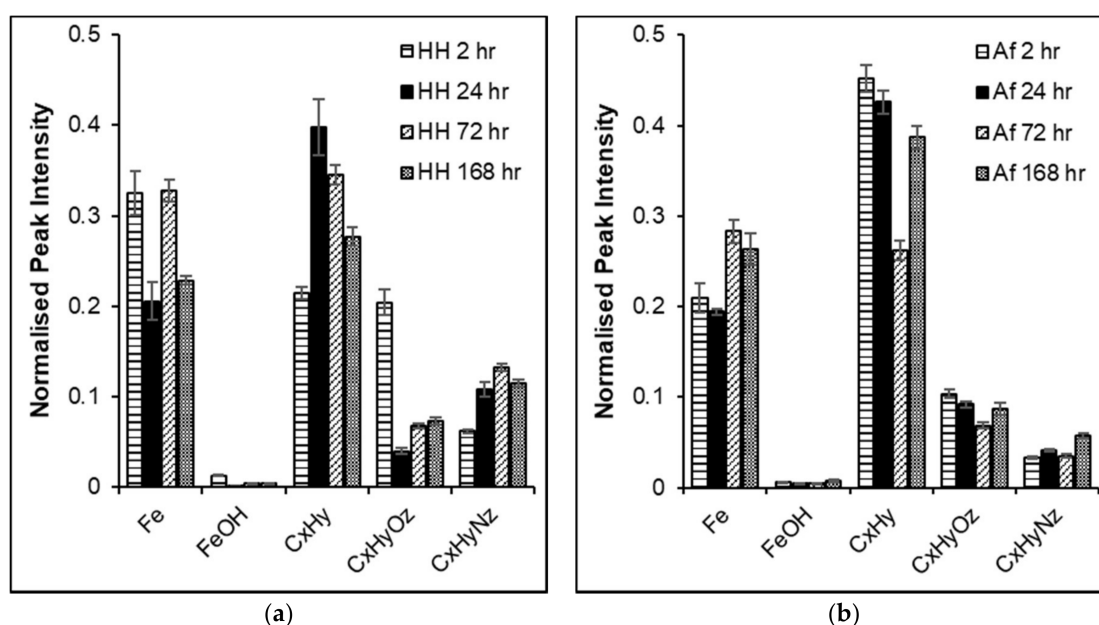

(**a**)   (**b**)

Figure 6. ToF-SIMS normalised peak intensities of positive ion fragments of pyrite exposed to: (**a**) HH medium for 2, 24, 72 and 168 h; and (**b**) *A. ferrooxidans* for 2, 24, 72 and 168 h. 95% confidence interval where n = 5.

The positive ion signals confirm that exposure of pyrite to *A. ferrooxidans* results in significant modification of the surface chemical speciation. The positive ion fragments are dominated by Fe and short chain C_xH_y ($x \leq 6$) over the course of exposure to HH medium and *A. ferrooxidans*. The Fe significantly increases at 72 h and remains constant at 168 h when exposed to *A. ferrooxidans*, while the Fe is variable for the controls. The FeOH fragment undergoes little variation in proportion on the surface over the course of exposure, indicating little to no jarosite formation on the surface, as confirmed by the SEM micrographs (Figure 6b). A comparison of samples exposed to *A. ferrooxidans* over time indicates the formation of N-containing organic species at 168 h. These results suggest the production of proteins in the biofilm at this time, and are supported by C K-edge NEXAFS results.
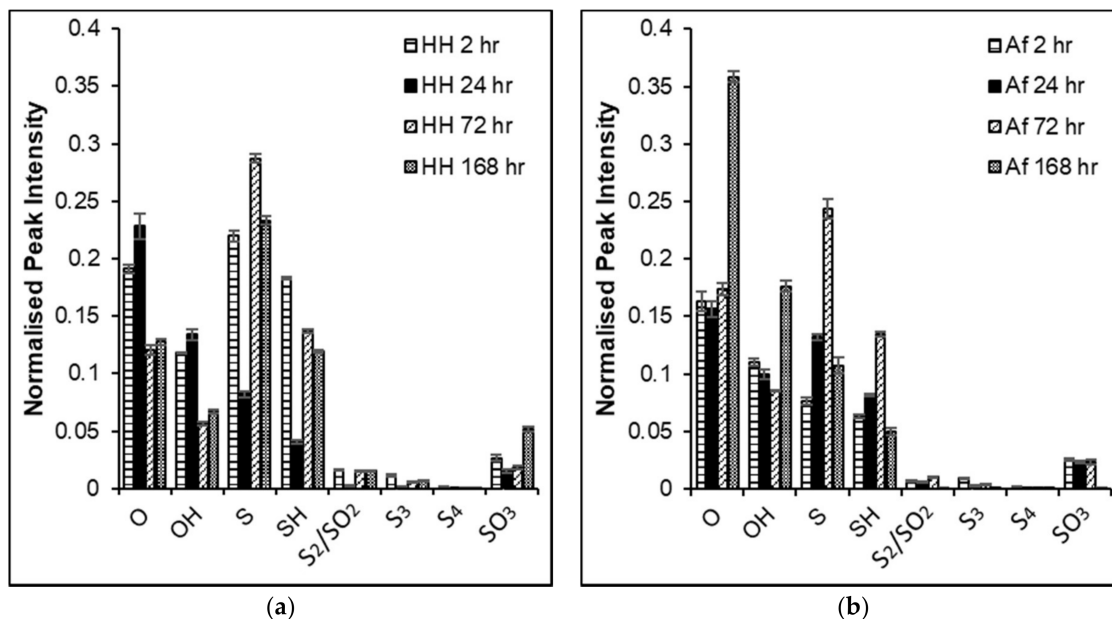
Figure 7. ToF-SIMS normalised peak intensities of negative ion fragments of pyrite exposed: (**a**) HH medium for 2, 24, 72 and 168 h; (**b**) *A. ferrooxidans* for 2, 24, 72 and 168 h. 95% confidence interval where n = 5.

The negative ion fragments suggest that there is some oxidation of surface to form S_2, S_3 and sulfur-oxy species during exposure to HH medium and *A. ferrooxidans*, Figure 7. The lower detection of S species at the surface of the samples exposed to *A. ferrooxidans* coupled with the higher C_xH_y speciation indicates the formation of an organic over-layer due to biofilm formation. These results show that the O and OH ions dominate the negative spectra, and overlap strongly with hydrocarbons produced by bacteria, in agreement with the findings of Pradier [52]. The hydrophobicity of the sample is dictated by a balance between the hydrophilic polysaccharides and Fe oxyhydroxides and hydrophobic proteins and sulfur polymeric surface species.

4. Discussion

Surface morphology studies comparing chemically leached pyrite tiles with those exposed to *A. ferrooxidans* have shown that the presence *A. ferrooxidans* accelerates the dissolution of the pyrite surface. The samples exposed to *A. ferrooxidans* exhibit large etch pits and rivers of crack along the surface by 168 h of exposure; while the chemical controls show little change in surface morphology. The low concentration of cells irreversibly attached to pyrite within 2 h, coupled with evidence of dissolution, indicate that direct contact between the bacteria and mineral surface is not required to oxidize the pyrite surface. As attachment to surfaces with roughness less than their cell size is thermodynamically unfavorable due to increased tension along the cell's membrane in regions where the bacterium is not in direct contact with the surface [86]. The polished pyrite tiles used in this study provide inadequate microscale topography for the bacteria to seek protection in large pits and voids, and form chemical attachment to the surface over time [86]. In this case, the adhesion of bacteria is primarily due to the local chemical environment and food source. The cells must excrete EPS to irreversibly attach to the mineral surface and form a biofilm.

Evidence of EPS was observed on the pyrite surface within 2 h via PEEM, ToF-SIMS and captive bubble contact angle measurements. The adsorption of EPS to the pyrite surface rendered it hydrophilic and allowed for binding of larger bacterial colonies by 168 h. The evolution of EPS and the biofilm chemistry show polysaccharide and fatty acid compounds are produced at early exposure stages, with protein and nucleic acid compounds being produced at longer exposure times. As a biofilm

begins to form on the surface, as was observed from the SEM images, more extracellular polymeric substances and fatty acids were produced by the cells. This increase in oxidation and formation of polysaccharide and fatty acids compounds promotes the hydrophilicity of the surface observed in the contact angle results. These results support the idea that the indirect contact mechanism is the dominant mechanism through which cells interact with the pyrite surface [53–55,87]. The anionic functional groups from proteins and polysaccharides including carboxyl, sulfydryl, glycerae and phosphate, bind with metals including iron. This allows for initial oxidation of pyrite to Fe^{3+}-EPS complexes without bacterial attachment [88,89]. The interaction of *A. ferrooxidans* can, therefore, be described as an indirect mechanism whereby EPS interacts with the pyrite surface, followed by an indirect contact mechanism as the cells irreversibly attach to the surface and biofilm develops [16,21,23].

One of the challenges still facing the application of microorganisms in bioflotation is the unknown costs, and the uncertainty regarding the amount of cellular material required to depress minerals [90]. As polysaccharides and fatty acids are produced at early exposure stages, cells or EPS-harvested at this period of exposure to pyrite are likely to be more beneficial to the potential depression of pyrite than the more hydrophobic protein- and nucleic acid-rich EPS produced at longer periods of exposure. These findings suggest that biofilm formation is not required to significantly decrease the hydrophobicity of pyrite. EPS produced by *A. ferrooxidans* during initial attachment and at low cell coverage of the surface is adequate for surface modification.

The EPS components produced by *A. ferrooxidans* have been observed in previous studies to contain a mixture of proteins, polysaccharides, uronic, humic and deoxyribonucleic acids [18–22], with the source of nutrients having been demonstrated to impact the composition and amount of EPS produced by cells [87]. These results suggest that the period of exposure to the mineral surface is a factor that must be considered in future applications of *A. ferrooxidans* to bioflotation.

5. Conclusions

Attachment of cells during the first hours of exposure was observed using SEM, with no obvious preference for surface defects. A biofilm develops after 168 h of exposure. The leaching of the pyrite is accelerated by the presence of bacteria, with the mineral surface showing more significant pitting than is caused by acidic medium alone. The difference in hydrophobicity is greatest between bacterial exposure and abiotic control after 2 h, which coincides with the presence of polysaccharide and fatty acid-type structures measured by PEEM. However, longer periods of exposure lead to inorganic oxidation of the pyrite surface, causing little difference in hydrophobicity of the samples until a biofilm begins to form after 168 h. These observations suggest that *A. ferrooxidans* preferentially produces polysaccharide and fatty acid compounds to assist with initial adhesion to pyrite, before beginning to produce more hydrophobic proteins as colonies begin to develop on the surface. This has important implications for the field of bioflotation, which would ideally require short-term exposure for the most efficient separation of minerals. This study suggests that the nature of bacterial excretions changes as the requirements of the cells change over time, and as such, the time cells are harvested and the length of exposure to the mineral is of crucial importance for effective separation of minerals.

Author Contributions: S.M.L.V., J.S.Q. and S.L.H. conceived and designed the experiments; S.M.L.V., K.N. and S.L.H. performed the experiments; S.M.L.V. analyzed the data; P.Y.C., Y.L.C., W.D.H. and S.L.H. and contributed reagents/materials/analysis tools; S.M.L.V., J.S.Q. and S.L.H. wrote the paper.

References

1.　Li, J.; Dabrowski, B.; Miller, J.D.; Acar, S.; Dietrich, M.; Le Vier, K.M.; Wan, R.Y. The influence of pyrite pre-oxidation on gold recovery by cyanidation. *Miner. Eng.* **2006**, *19*, 883–895. [CrossRef]

2.　Hodgkinson, G.; Sandenberght, R.F.; Hunter, C.J.; De Wet, J.R. Pyrite flotation from gold leach residues. *Miner. Eng.* **1994**, *7*, 691–698. [CrossRef]

3.　Yan, D.S. Selective flotation of pyrite and gold tellurides. *Miner. Eng.* **1997**, *10*, 327–337. [CrossRef]

4.　Mu, Y.; Peng, Y.; Lauten, R.A. The depression of pyrite in selective flotation by different reagent systems—A literature review. *Miner. Eng.* **2016**, *96*, 143–156. [CrossRef]

5.　Wills, B.A. *Wills' Mineral Processing Technology*, 7th ed.; Elsevier: Oxford, UK, 2006; p. 444.

6.　Nagaraj, D.R. Minerals recovery and processing. In *Kirk-Othmer Encyclopedia of Chemical Technology*; John Wiley & Sons, Inc.: Hoboken, NJ, USA, 2000; Volume 16, pp. 595–679.

7.　Kawatra, S.K. Flotation fundamentals. In *Mining Engineering Handbook*; Michigan Technological University: Houghton, MI, USA, 2009; p. 30.

8.　Fuerstenau, M.C.; Chander, S.; Woods, R. Sulphide mineral flotation. In *Froth Flotation: A Century of Innovation*; Fuerstenau, M.C., Jameson, G., Yoon, R.-H., Eds.; Society for Mining, Metallurgy, and Exploration: Littleton, CO, USA, 2007; pp. 425–464.

9.　Farahat, M.; Hirajima, T.; Sasaki, K.; Aiba, Y.; Doi, K. Adsorption of sip e. Coli onto quartz and its applications in froth flotation. *Miner. Eng.* **2008**, *21*, 389–395. [CrossRef]

10.　Langwaldt, J.; Kalapudas, R. Bio-benefication of multimetal black shale ore by flotation. *Physico. Probl. Miner. Process.* **2007**, *41*, 291–299.

11.　Mehrabani, J.V.; Mousavi, S.M.; Noaparast, M. Evaluation of the replacement of nacn with acidithiobacillus ferrooxidans in the flotation of high-pyrite, low-grade lead–zinc ore. *Sep. Purif. Technol.* **2011**, *80*, 202–208. [CrossRef]

12.　Smith, R.W.; Miettinen, M. Microorganisms in flotation and flocculation: Future technology or laboratory curiosity? *Miner. Eng.* **2006**, *19*, 548–553. [CrossRef]

13.　Rao, H.K.; Vilinska, A.; Chernyshova, I.V. Minerals bioprocessing: R & d needs in mineral biobeneficiation. *Hydrometallurgy* **2010**, *104*, 465–470.

14.　Mehrabani, J.V.; Noaparast, M.; Mousavi, S.M.; Dehghan, R.; Rasooli, E.; Hajizadeh, H. Depression of pyrite in the flotation of high pyrite low-grade lead–zinc ore using acidithiobacillus ferrooxidans. *Miner. Eng.* **2010**, *23*, 10–16. [CrossRef]

15.　Chandraprabha, M.N.; Natarajan, K.A.; Somasundaran, P. Selective separation of pyrite from chalcopyrite and arsenopyrite by biomodulation using acidithiobacillus ferrooxidans. *Int. J. Miner. Process.* **2005**, *75*, 113–122. [CrossRef]

16.　Crundwell, F.K. How do bacteria interact with minerals? *Hydrometallurgy* **2003**, *71*, 75–81. [CrossRef]

17.　Sand, W.; Gehrke, T.; Jozsa, P.-G.; Schippers, A. (Bio)chemistry of bacterial leaching—Direct vs. Indirect bioleaching. *Hydrometallurgy* **2001**, *59*, 159–175. [CrossRef]

18.　Kinzler, K.; Gehrke, T.; Telegdi, J.; Sand, W. Bioleaching—A result of interfacial processes caused by extracellular polymeric substances (eps). *Hydrometallurgy* **2003**, *71*, 83–88. [CrossRef]

19.　Comte, S.; Guibaud, G.; Baudu, M. Relations between extraction protocols for activated sludge extracellular polymeric substances (eps) and eps complexation properties: Part i. Comparison of the efficiency of eight eps extraction methods. *Enzyme Microb. Technol.* **2006**, *38*, 237–245. [CrossRef]

20.　Sharma, P.K.; Das, A.; Hanumantha Rao, K.; Forssberg, K.S.E. Surface characterization of acidithiobacillus ferrooxidans cells grown under different conditions. *Hydrometallurgy* **2003**, *71*, 285–292. [CrossRef]

21.　Watling, H.R. The bioleaching of sulphide minerals with emphasis on copper sulphides—A review. *Hydrometallurgy* **2006**, *84*, 81–108. [CrossRef]

22.　Rohwerder, T.; Sand, W. Mechanisms and biochemical fundamentals of bacterial metal sulfide oxidation. In *Microbial Processing of Metal Sulfides*; Sand, E.R.D.A.W., Ed.; Springer: Berlin, Germany, 2007; pp. 35–58.

23.　Harneit, K.; Göksel, A.; Kock, D.; Klock, J.H.; Gehrke, T.; Sand, W. Adhesion to metal sulfide surfaces by cells of acidithiobacillus ferrooxidans, acidithiobacillus thiooxidans and leptospirillum ferrooxidans. *Hydrometallurgy* **2006**, *83*, 245–254. [CrossRef]

24. Poorni, S.; Natarajan, K.A. Flocculation behaviour of hematite–kaolinite suspensions in presence of extracellular bacterial proteins and polysaccharides. *Coll. Surf. B Biointerfaces* **2014**, *114*, 186–192. [CrossRef] [PubMed]

25. Vilinska, A.; Hanumantha Rao, K. Leptospirillum ferrooxidans-sulfide mineral interactions with reference to bioflotation and bioflocculation. *Trans. Nonferrous Met. Soc. China* **2008**, *18*, 1403–1409. [CrossRef]

26. Dague, E.; Delcorte, A.; Latgé, J.P.; Dufrêne, Y.F. Combined use of atomic force microscopy, X-ray photoelectron spectroscopy, and secondary ion mass spectrometry for cell surface analysis. *Langmuir* **2008**, *24*, 2955–2959. [CrossRef] [PubMed]

27. Stohr, J. *Nexafs Spectroscopy*; Springer-Verlag: Berlin/Heidelberg, Germany, 1992; Volume 25, p. 404.

28. Wei, D.H.; Chan, Y.L.; Hsu, Y.J. Exploring the magnetic and organic microstructures with photoemission electron microscope. *J. Electron Spectrosc. Relat. Phenom.* **2012**, *185*, 429–435. [CrossRef]

29. Wei, D.H.; Hsu, Y.J.; Klauser, R.; Hong, I.H.; Yin, G.C.; Chuang, T.J. Photoelectron microscopy projects at srrc. *Surf. Rev. Lett.* **2003**, *10*, 617–624.

30. Acres, R.G.; Harmer, S.L.; Beattie, D.A. Synchrotron peem and tof-sims study of oxidized heterogenous pentlandite, pyrrhotite and chalcopyrite. *J. Synchrotron Radiat.* **2010**, *17*, 606–615. [PubMed]

31. Acres, R.G.; Harmer, S.L.; Beattie, D.A. Synchrotron xps, nexafs, and tof-sims studies of solution exposed chalcopyrite and heterogeneous chalcopyrite with pyrite. *Miner. Eng.* **2010**, *23*, 928–936. [CrossRef]

32. Belu, A.M.; Graham, D.J.; Castner, D.G. Time-of-flight secondary ion mass spectrometry: Techniques and applications for the characterization of biomaterial surfaces. *Biomaterials* **2003**, *24*, 3635–3653. [CrossRef]

33. Briggs, D.; Vickerman, J.C. *Tof-Sims: Surface Analysis by Mass Spectrometry*; SurfaceSpectra Chichester: Manchester, UK, 2001.

34. Belu, A.M.; Davies, M.C.; Newton, J.M.; Patel, N. Tof-sims characterization and imaging of controlled-release drug delivery systems. *Anal. Chem.* **2000**, *72*, 5625–5638. [CrossRef] [PubMed]

35. Berman, E.S.F.; Kulp, K.S.; Knize, M.G.; Wu, L.; Nelson, E.J.; Nelson, D.O.; Wu, K.J. Distinguishing monosaccharide stereo- and structural isomers with tof-sims and multivariate statistical analysis. *Anal. Chem.* **2006**, *78*, 6497–6503. [CrossRef] [PubMed]

36. De Brouwer, J.F.C.; Cooksey, K.E.; Wigglesworth-Cooksey, B.; Staal, M.J.; Stal, L.J.; Avci, R. Time of flight-secondary ion mass spectrometry on isolated extracellular fractions and intact biofilms of three species of benthic diatoms. *J. Microbiol. Methods* **2006**, *65*, 562–572. [CrossRef] [PubMed]

37. Murphy, R.; Strongin, D.R. Surface reactivity of pyrite and related sulfides. *Surf. Sci. Rep.* **2009**, *64*, 1–45. [CrossRef]

38. Franzblau, R.E.; Daughney, C.J.; Swedlund, P.J.; Weisener, C.G.; Moreau, M.; Johannessen, B.; Harmer, S.L. Cu(IIii) removal by anoxybacillus flavithermus–iron oxide composites during the addition of Fe(II)aq. *Geochimica et Cosmochimica Acta* **2016**, *172*, 139–158. [CrossRef]

39. Bui, L.M.G.; Turnidge, J.D.; Kidd, S.P. The induction of staphylococcus aureus biofilm formation or small colony variants is a strain-specific response to host-generated chemical stresses. *Microbes Infect.* **2015**, *17*, 77–82. [CrossRef] [PubMed]

40. Tan, S.N.; Chen, M. Early stage adsorption behaviour of acidithiobacillus ferrooxidans on minerals I: An experimental approach. *Hydrometallurgy* **2012**, *119*, 87–94. [CrossRef]

41. Read, M.L.; Morgan, P.B.; Kelly, J.M.; Maldonado-Codina, C. Dynamic contact angle analysis of silicone hydrogel contact lenses. *J. Biomater. Appl.* **2010**, *26*, 85–99. [CrossRef] [PubMed]

42. Campbell, D.; Carnell, S.M.; Eden, R.J. Applicability of contact angle techniques used in the analysis of contact lenses, part 1: Comparative methodologies. *Eye Contact Lens* **2013**, *39*, 254–262. [CrossRef] [PubMed]

43. Beaussart, A.; Mierczynska-Vasilev, A.M.; Harmer, S.L.; Beattie, D.A. The role of mineral surface chemistry in modified dextrin adsorption. *J. Colloid Interface Sci.* **2011**, *357*, 510–520. [CrossRef] [PubMed]

44. Yin, G.C.; Wei, D.H.; Hsu, Y.J.; Tsang, K.L. The Image Acquisition and Analysis Program for Peem Station. In *Proceedings of the AIP Conference Proceedings, San Fransisco, California, USA, 25–29 August 2003*; American Institute of Physics: College Park, MD, USA, 2004; p. 897.

45. Goh, S.W.; Buckley, A.N.; Lamb, R.N.; Rosenberg, R.A.; Moran, D. The oxidation states of copper and iron in mineral sulfides, and the oxides formed on initial exposure of chalcopyrite and bornite to air. *Geochim. Cosmochim. Acta* **2006**, *70*, 2210–2228. [CrossRef]

46. Brandes, J.A.; Cody, G.D.; Rumble, D.; Haberstroh, P.; Wirick, S.; Gelinas, Y. Carbon k-edge xanes spectromicroscopy of natural graphite. *Carbon* **2008**, *46*, 1424–1434. [CrossRef]

47. Hitchcock, A.P.; Morin, C.; Zhang, X.; Araki, T.; Dynes, J.J.; Stöver, H.; Brash, J.; Lawrence, J.R.; Leppard, G.G. Soft X-ray spectromicroscopy of biological and synthetic polymer systems. *J. Electron Spectrosc. Relat. Phenom.* **2005**, *144*, 259–269. [CrossRef]

48. Hitchcock, A.P.; Morin, C.; Heng, Y.M.; Cornelius, R.M.; Brash, J.L. Towards practical soft X-ray spectromicroscopy of biomaterials. *J. Biomater. Sci. Polym. Ed.* **2002**, *13*, 919–937. [CrossRef] [PubMed]

49. Ravel, B.; Newville, M. Athena, artemis, hephaestus: Data analysis for X-ray absorption spectroscopy using ifeffit. *J. Synchrotron Radiat.* **2005**, *12*, 537–541. [CrossRef] [PubMed]

50. Smart, R.S.C.; Jasieniak, M.; Prince, K.E.; Skinner, W.M. Sims studies of oxidation mechanisms and polysulfide formation in reacted sulfide surfaces. *Miner. Eng.* **2000**, *13*, 857–870. [CrossRef]

51. Piantadosi, C.; Smart, R.S.C. Statistical comparison of hydrophobic and hydrophilic species on galena and pyrite particles in flotation concentrates and tails from tof-sims evidence. *Int. J. Miner. Process.* **2002**, *64*, 43–54. [CrossRef]

52. Pradier, C.M.; Rubio, C.; Poleunis, C.; Bertrand, P.; Marcus, P.; Compère, C. Surface characterization of three marine bacterial strains by fourier transform ir, X-ray photoelectron spectroscopy, and time-of-flight secondary-ion mass spectrometry, correlation with adhesion on stainless steel surfaces. *J. Phys. Chem. B* **2005**, *109*, 9540–9549. [CrossRef] [PubMed]

53. Gleisner, M.; Herbert, R.B.; Frogner Kockum, P.C. Pyrite oxidation by acidithiobacillus ferrooxidans at various concentrations of dissolved oxygen. *Chem. Geol.* **2006**, *225*, 16–29. [CrossRef]

54. Liu, H.; Gu, G.; Xu, Y. Surface properties of pyrite in the course of bioleaching by pure culture of acidithiobacillus ferrooxidans and a mixed culture of acidithiobacillus ferrooxidans and acidithiobacillus thiooxidans. *Hydrometallurgy* **2011**, *108*, 143–148. [CrossRef]

55. Yu, J.-Y.; McGenity, T.J.; Coleman, M.L. Solution chemistry during the lag phase and exponential phase of pyrite oxidation by thiobacillus ferrooxidans. *Chem. Geol.* **2001**, *175*, 307–317. [CrossRef]

56. Karavaiko, G.I.; Smolskaja, L.S.; Golyshina, O.K.; Jagovkina, M.A.; Egorova, E.Y. Bacterial pyrite oxidation: Influence of morphological, physical and chemical properties. *Fuel Process. Technol.* **1994**, *40*, 151–165. [CrossRef]

57. Edwards, K.J.; Rutenberg, A.D. Microbial response to surface microtopography: The role of metabolism in localized mineral dissolution. *Chem. Geol.* **2001**, *180*, 19–32. [CrossRef]

58. Mitsunobu, S.; Zhu, M.; Takeichi, Y.; Ohigashi, T.; Suga, H.; Jinno, M.; Makita, H.; Sakata, M.; Ono, K.; Mase, K.; et al. Direct detection of Fe(ii) in extracellular polymeric substances (eps) at the mineral-microbe Interface in bacterial pyrite leaching. *Microbes Environ.* **2016**, *31*, 63–69. [CrossRef] [PubMed]

59. Xia, J.L.; Yang, Y.; He, H.; Zhao, X.J.; Liang, C.L.; Zheng, L.; Ma, C.Y.; Zhao, Y.D.; Nie, Z.Y.; Qiu, G.Z. Surface analysis of sulfur speciation on pyrite bioleached by extreme thermophile acidianus manzaensis using raman and xanes spectroscopy. *Hydrometallurgy* **2010**, *100*, 129–135. [CrossRef]

60. Vilinska, A.; Hanumantha Rao, K. Surface thermodynamics and extended dlvo theory of acidithiobacillus ferrooxidans cells adhesion on pyrite and chalcopyrite. *Open Colloid Sci. J.* **2009**, *2*, 1–14. [CrossRef]

61. Ohmura, N.; Kitamura, K.; Saiki, H. Selective adhesion of thiobacillus ferrooxidans to pyrite. *Appl. Environ. Microbiol.* **1993**, *59*, 4044–4050. [PubMed]

62. Nagaoka, T.; Ohmura, N.; Saiki, H. A novel mineral processing by flotation using thiobacillus ferrooxidans. In *Process Metallurgy*; Amils, R., Ballester, A., Eds.; Elsevier: Amsterdam, The Nertherlands, 1999; Volume 9, pp. 335–342.

63. Womes, M.; Karnatak, R.C.; Esteva, J.M.; Lefebvre, I.; Allan, G.; Olivier-Fourcades, J.; Jumas, J.C. Electronic structures of FeS and FeS$_2$: X-ray absorption spectroscopy and band structure calculations. *J. Phys. Chem. Solids* **1997**, *58*, 345–352. [CrossRef]

64. Fleet, M.E. Xanes spectroscopy of sulphur in earth materials. *Can. Miner.* **2005**, *43*, 1811–1838. [CrossRef]

65. Von Oertzen, G.U.; Jones, R.T.; Gerson, A.R. Electronic and optical properties of Fe, Zn and Pb sulfides. *Phys. Chem. Miner.* **2005**, *32*, 255–268. [CrossRef]

66. Miedema, P.S.; de Groot, F.M.F. The iron l edges: Fe 2p X-ray absorption and electron energy loss spectroscopy. *J. Electron Spectrosc. Relat. Phenom.* **2013**, *187*, 32–48. [CrossRef]

67. Van Aken, P.A.; Lauterbach, S. Strong magnetic linear dichroism in Fe L_{23} and O K electron energy-loss near-edge spectra of antiferromagnetic hematite α-Fe$_2$O$_3$. *Phys. Chem. Miner.* **2003**, *30*, 469–477. [CrossRef]

68. Van Aken, P.A.; Liebscher, B. Quantification of ferrous/ferric ratios in minerals: New evaluation schemes of Fe L_{23} electron energy-loss near-edge spectra. *Phys. Chem. Miner.* **2002**, *29*, 188–200. [CrossRef]

69. Doyle, C.S.; Kendelewicz, T.; Bostick, B.C.; Brown, G.E. Soft X-ray spectroscopic studies of the reaction of fractured pyrite surfaces with Cr(vi)-containing aqueous solutions. *Geochim. Cosmochim. Acta* **2004**, *68*, 4287–4299. [CrossRef]

70. Kalegowda, Y.; Harmer, S.L. Classification of time-of-flight secondary ion mass spectrometry spectra from complex Cu-Fe sulphides by principal component analysis and artificial neural networks. *Anal. Chim. Acta* **2013**, *759*, 21–27. [CrossRef] [PubMed]

71. Kalegowda, Y.; Chan, Y.L.; Wei, D.H.; Harmer, S.L. X-peem, xps and tof-sims characterisation of xanthate induced chalcopyrite flotation: Effect of pulp potential. *Surf. Sci.* **2015**, *635*, 70–77. [CrossRef]

72. Buckley, A.N.; Woods, R. An X-ray photoelectron spectroscopic study of the oxidation of chalcopyrite. *Aust. J. Chem.* **1984**, *37*, 2403–2413. [CrossRef]

73. Kaznacheyev, K.; Osanna, A.; Jacobsen, C.; Plashkevych, O.; Vahtras, O.; Ågren, H.; Carravetta, V.; Hitchcock, A.P. Innershell absorption spectroscopy of amino acids. *J. Phys. Chem. A* **2002**, *106*, 3153–3168. [CrossRef]

74. Stewart-Ornstein, J.; Hitchcock, A.P.; Hernandez Cruz, D.; Henklein, P.; Overhage, J.; Hilpert, K.; Hale, J.D.; Hancock, R.E. Using intrinsic X-ray absorption spectral differences to identify and map peptides and proteins. *J. Phys. Chem. B* **2007**, *111*, 7691–7699. [CrossRef] [PubMed]

75. Solomon, D.; Lehmann, J.; Harden, J.; Wang, J.; Kinyangi, J.; Heymann, K.; Karunakaran, C.; Lu, Y.; Wirick, S.; Jacobsen, C. Micro- and nano-environments of carbon sequestration: Multi-element stxm–nexafs spectromicroscopy assessment of microbial carbon and mineral associations. *Chem. Geol.* **2012**, *329*, 53–73. [CrossRef]

76. Wan, J.; Tyliszczak, T.; Tokunaga, T.K. Organic carbon distribution, speciation, and elemental correlations within soil microaggregates: Applications of stxm and nexafs spectroscopy. *Geochim. Cosmochim. Acta* **2007**, *71*, 5439–5449. [CrossRef]

77. Miot, J.; Benzerara, K.; Morin, G.; Kappler, A.; Bernard, S.; Obst, M.; Férard, C.; Skouri-Panet, F.; Guigner, J.-M.; Posth, N.; et al. Iron biomineralization by anaerobic neutrophilic iron-oxidizing bacteria. *Geochim. Cosmochim. Acta* **2009**, *73*, 696–711. [CrossRef]

78. Rightor, E.G.; Hitchcock, A.P.; Ade, H.; Leapman, R.D.; Urquhart, S.G.; Smith, A.P.; Mitchell, G.; Fischer, D.; Shin, H.J.; Warwick, T. Spectromicroscopy of poly(ethylene terephthalate): Comparison of spectra and radiation damage rates in X-ray absorption and electron energy loss. *J. Phys. Chem. B* **1997**, *101*, 1950–1960. [CrossRef]

79. Zubavichus, Y.; Fuchs, O.; Weinhardt, L.; Heske, C.; Umbach, E.; Denlinger, J.D.; Grunze, M. Soft X-ray-induced decomposition of amino acids: An xps, mass spectrometry, and nexafs study. *Radiat. Res.* **2004**, *161*, 346–358. [CrossRef] [PubMed]

80. Watts, B.; Thomsen, L.; Dastoor, P.C. Methods in carbon k-edge nexafs: Experiment and analysis. *J. Electron Spectrosc. Relat. Phenom.* **2006**, *151*, 105–120. [CrossRef]

81. Dynes, J.J.; Lawrence, J.R.; Korber, D.R.; Swerhone, G.D.; Leppard, G.G.; Hitchcock, A.P. Morphological and biochemical changes in pseudomonas fluorescens biofilms induced by sub-inhibitory exposure to antimicrobial agents. *Can. J. Microbiol.* **2009**, *55*, 163–178. [CrossRef] [PubMed]

82. Boese, J.; Osanna, A.; Jacobsen, C.; Kirz, J. Carbon edge xanes spectroscopy of amino acids and peptides. *J. Electron Spectrosc. Relat. Phenom.* **1997**, *85*, 9–15. [CrossRef]

83. Coker, V.S.; Byrne, J.M.; Telling, N.D.; Van Der Laan, G.; Lloyd, J.R.; Hitchcock, A.P.; Wang, J.; Pattrick, R.A.D. Characterisation of the dissimilatory reduction of fe(iii)-oxyhydroxide at the microbe—Mineral interface: The application of stxm–xmcd. *Geobiology* **2012**, *10*, 347–354. [CrossRef] [PubMed]

84. Morin, C.; Hitchcock, A.P.; Cornelius, R.M.; Brash, J.L.; Urquhart, S.G.; Scholl, A.; Doran, A. Selective adsorption of protein on polymer surfaces studied by soft X-ray photoemission electron microscopy. *J. Electron Spectrosc. Relat. Phenom.* **2004**, *137*, 785–794. [CrossRef]

85. Chan, C.S.; Fakra, S.C.; Edwards, D.C.; Emerson, D.; Banfield, J.F. Iron oxyhydroxide mineralization on microbial extracellular polysaccharides. *Geochim. Cosmochim. Acta* **2009**, *73*, 3807–3818. [CrossRef]

86. Lillian, C.; Hsu, A.; Jean Fang, B.; Diana, A.; Borca-Tasciuc, C.; Randy, W.; Worobo, A.; Carmen, I. Morarua effect of micro- and nanoscale topography on the adhesion of bacterial cells to solid surfaces. *Appl. Environ. Microbiol.* **2013**, *79*, 2703–2712.

87. Li, Q.; Wang, Q.; Zhu, J.; Zhou, S.; Gan, M.; Jiang, H.; Sand, W. Effect of extracellular polymeric substances on surface properties and attachment behavior of acidithiobacillus ferrooxidans. *Minerals* **2016**, *6*, 100. [CrossRef]

88. Beech, I.B.; Sunner, J. Biocorrosion: Towards understanding interactions between biofilms and metals. *Curr. Opin. Biotechnol.* **2004**, *15*, 181–186. [CrossRef] [PubMed]

89. Rojas-Chapana, J.A.; Tributsch, H. Bio-leaching of pyrite accelerated by cysteine. *Process Biochem.* **2000**, *35*, 815–824. [CrossRef]

90. Otsuki, A.; Ohshima, H. Use of microorganisms for complex ore beneficiation: Bioflotation as an example. In *Encyclopedia of Biocolloid and Biointerface Science 2v Set*; John Wiley & Sons, Inc.: Hoboken, NJ, USA, 2016; pp. 108–117.